Sikora *et al. Int J Concr Struct Mater (2023) 17:7*
https://doi.org/10.1186/s40069-022-00568-y

International Journal of Concrete Structures and Materials

RESEARCH Open Access

# Rheological, Mechanical, Microstructural and Radiation Shielding Properties of Cement Pastes Containing Magnetite ($Fe_3O_4$) Nanoparticles

Pawel Sikora[1,2*], Ahmed M. El-Khayatt[3,4], H. A. Saudi[5], Maxime Liard[6], Didier Lootens[6], Sang-Yeop Chung[7*], Paweł Woliński[8] and Mohamed Abd Elrahman[9]

**Abstract**

This work examines the influence of iron oxide nanoparticles ($Fe_3O_4$ NPs) on neutron and gamma-ray radiation shielding characteristics of Portland cement paste. Experimental evaluations were supplemented with theoretical studies using NXCom program. Portland cement pastes with 5, 10, 15, 20, and 30 wt% of nanomagnetite cement replacement were produced. Moreover, rheological, early strength development, compressive strength, and mercury intrusion porosimetry (MIP) tests were performed. The results showed that increasing the amount of $Fe_3O_4$ NPs in a mix leads to a gradual increment in measured viscosity and yield stress. High nano-$Fe_3O_4$ content substantially impeded the early strength development process and led to a decrement in the 7- and 28-day compressive strength of cement paste. The MIP studies exhibited a gradual increment in total porosity, and average pore volume, as nano-$Fe_3O_4$ content was increased. All the macroscopic cross-sections of slow, fast and thermal neutrons constantly increased as a result of the addition of magnetite nanoparticles, with their variations being markedly linear. Similarly, gamma attenuation test results indicated that the addition of $Fe_3O_4$ powder enhances the shielding capability of paste in the energy range of interest (0.08–2.614 MeV). In conclusion, $Fe_3O_4$ nanoparticles can be successfully used in producing lead-free cementitious composites with improved gamma-ray and neutron shielding properties. However, certain drawbacks related to an increment in matrix porosity and thus a decrement in mechanical performance should be taken into account.

**Keywords:** Cement, Gamma-ray shielding, Neutron shielding, Nanomagnetite, $Fe_3O_4$, Rheology

## 1 Introduction

Concrete is one of the most widely used materials in radiation (biological) shielding. Its popularity can be attributed to an acceptable price, relative freedom in terms of geometry (casting), as well as high material design versatility, which gives it much potential for incorporating a great variety of waste and secondary raw materials (Mohamed et al. 2022; Ramadan et al. 2020). It is used for radiation protection in radiation therapy facilities, nuclear reactors as well as in military applications (Radziejowska et al. 2021). To date, many approaches aimed towards improving the radiation shielding properties of concrete have been proposed; including the selection of the proper aggregate type (Jóźwiak-Niedźwiedzka et al. 2018), as well as the proper additives and admixtures (Piotrowski 2021). In general, materials such as

Journal information: ISSN 1976-0485 / eISSN 2234-1315

*Correspondence: pawel.sikora@zut.edu.pl; sychung@sejong.ac.kr

[2] Faculty of Civil and Environmental Engineering, West Pomeranian University of Technology in Szczecin, Al. Piastow 50, 70-311 Szczecin, Poland
[7] Department of Civil and Environmental Engineering, Sejong University, Seoul 05006, South Korea
Full list of author information is available at the end of the article

lead (Pb), with a high atomic number (high-Z), are preferred for absorbing ionizing radiation (Saudi 2013). However, with growing concerns regarding the safety and potentially hazardous effects of lead, there has been substantial interest in developing of lead-free radiation shielding materials (Al-Rajhi et al. 2021). In recent years, special attention has particularly been paid to nanosized admixtures, which lead to far greater improvements in cementitious systems, compared to their micro-sized counterparts (Ghazanlou et al. 2020; Seifan et al. 2020; Sikora et al. 2021a). The beneficial effects of nanoparticles (NPs) are attributable to either their chemical activity, which supports the cement hydration process, or the filling effect, which improves the packing of the material within a matrix as a result of ultra-fine material size (Amin et al. 2015; El-Gamal et al. 2018; Kropyvnytska et al. 2019; Maher et al. 2021).

To produce lead-free radiation shielding cement composites, various high-Z NPs are used. These include $Bi_2O_3$, $TiO_2$, $Fe_2O_3$, and $Fe_3O_4$ (Abo-El-Enein et al. 2018; Dezhampanah et al. 2021; Sikora et al. 2021b). To date, $Fe_3O_4$ (nanomagnetite) has been found to be the most versatile in concrete applications (Horszczaruk 2019; Mansouri et al. 2019). This is because it can be used to facilitate the formation of concrete with various properties, including self-sensing (Piro et al. 2021) and self-healing (Seifan et al. 2018; Shaheen et al. 2019). Moreover, due to its highly magnetic properties, when added to cement-based composites, nano-$Fe_3O_4$ can be used as an electromagnetic wave absorber (He et al. 2018; Lesbayev et al. 2017), or as a rheology controlling agent under a magnetic field (Jiao et al., 2020, 2021).

In the vast majority of the available studies related to the incorporation of nano-$Fe_3O_4$ particles into cement-based composites, the amount of the material is limited up to 5 wt%, to ensure proper homogenous dispersion of the material within the matrix and thus facilitate the hydration process of the cementitious system (Akyildiz 2021; Amin et al. 2013; Bragança et al. 2016; Othuman Mydin et al. 2022; Sikora et al. 2018; Ślosarczyk et al. 2021). However, higher replacement rates would be expected to ensure a satisfactory amount of the material with a high atomic number to increase the radiation shielding potential of cementitious composites.

To date, only a limited number of publications related to the radiation shielding characteristics of cement-based composites containing nanomagnetite, are available. Horszczaruk et al. (2017) have experimentally evaluated the effects of adding 5 wt% and 10 wt% nano-$Fe_3O_4$ to cement pastes, in relation to gamma-ray against the monoenergetic photon energy of 0.662 MeV emitted by Cs-137. Only a slight increment in the linear attenuation coefficient (LAC) of cement paste, in ambient conditions and after exposure to elevated temperature (up to 450 °C), was reported. Florez et al. (2019) have experimentally evaluated the effects of nanomagnetite, used as a cement replacement at up to 50 wt% with only one energy level (0.662 MeV ($^{137}$Cs)), together with support from numerical studies (MCNP simulations). They reported a compressive strength loss in nanomagnetite-modified specimens when the addition of nano-$Fe_3O_4$ exceeded 10 wt%. Similarly, a gradual decrement in gamma-ray attenuation was reported when the NP content exceeded 10 wt%. However, it is worth noting that the authors did not consider NPs to be binder materials and that the water-to-cement ratio (w/c) was set at a fixed value of w/c = 0.4). This resulted in a substantially lower amount of water in the specimens containing a high volume of NPs; therefore, a gradual decrement in specimen density was reported when the nano-$Fe_3O_4$ content was equal to or higher than 10 wt%.

Nevertheless, despite the availability of a few studies related to the gamma-ray attenuation properties of cement-based composites, it is clear that the available experimental data are limited only to one photon energy level (0.662 MeV), with there being no available data related to neutron attenuation. Moreover, minimal knowledge on the effects of high dosages of nano-$Fe_3O_4$ on the rheological, physico-mechanical and microstructural properties of cement pastes is available. Therefore, it is crucial to understand how high dosages of nano-$Fe_3O_4$ affect the engineering properties of cement-based composites, despite radiation shielding, towards proper concrete design.

This work aims at filling the gap in the existing knowledge. The proposed comprehensive experimental plan provides insight into producing a lead-free Portland cement-based shielding material evaluating the broad spectra of cement replacement with nano-$Fe_3O_4$ particles (from 5 wt% to 30 wt%). Fundamental cement pastes characteristics were determined (rheological, mechanical, microstructural) along with radiation shielding properties of Portland cement paste. Both experimental and theoretical evaluations of gamma-rays, fast and slow thermal neutrons, on the shielding properties of Portland cement composite pastes, were undertaken and correlated with other composite properties. As an outcome, a set of lead-free cement paste formulations are proposed below.

## 2 Materials and Mixture Design

### 2.1 Materials

Portland cement (CEM I 42.5 R), conforming to European standard EN 197–1, was used to produce the cement pastes in this study. The chemical compositions

**Table 1** Chemical composition and physical properties of cement [wt%]

| Material | CaO | $SiO_2$ | $Al_2O_3$ | $Fe_2O_3$ | MgO | $Na_2O$ | $K_2O$ | $SO_3$ | Blaine fineness [$cm^2/g$] | Density [$g/cm^3$] |
|---|---|---|---|---|---|---|---|---|---|---|
| CEM I 42.5 R | 63.14 | 20.53 | 5.33 | 2.36 | 1.49 | 0.21 | 0.72 | 3.39 | 5780 | 3.14 |

**Table 2** $Fe_3O_4$ nanopowder properties (data provided by supplier)

| Material | SEM particle size [nm] | BET surface area [$m^2/g$] | Specific gravity [$g/cm^3$] | Bulk density [$g/cm^3$] | Color |
|---|---|---|---|---|---|
| $Fe_3O_4$ nanopowder | 50–100 nm | 6–8 | 4.8–5.1 | 0.84 g/mL | Black |

and physical properties of CEM I 42.5 R are summarized in Table 1.

Commercially available magnetite ($Fe_3O_4$) nanopowder, purchased from Sigma Aldrich (637106), was used as received. The supplier data are summarized in Table 2. Scanning electron microscope (SEM, Zeiss GeminiSEM500 NanoVP) analysis confirmed the cubical shape of the $Fe_3O_4$ nanopowder, with a primary particle size of 50–100 nm (Fig. 1a-b). Similar data, obtained with the laser diffraction technique (Malvern Mastersizer 2000, UK) confirmed that the particle size distribution of the material was within that range (Fig. 1c). Powder D50 was found to have a particle size of 69 nm, while that of powder D90 was 136 nm in size. An X-ray diffraction study (Fig. 1d), performed with a PRO X-ray diffractometer (X'Pert PRO Philips diffractometer, Co. Ka radiation, Almelo, Holland), confirmed the presence of magnetite phase with seven characteristic diffraction peaks, corresponding to the standard card—JCPDS 19–629: 30.28 (30.14); 35.70 (35.52); 37.29 (37.0); 43.06 (43.31); 53.49 (53.7); 56.98 (57.28) and 62.75 (62.53). The specific gravity of the nano-$Fe_3O_4$, determined with a helium pycnometer, was found to be 5.0193 $g/cm^3$, which is in line with the range of the supplier's data. Additional information on the materials used can be found in other studies (Cendrowski et al. 2017; Sikora et al. 2016).

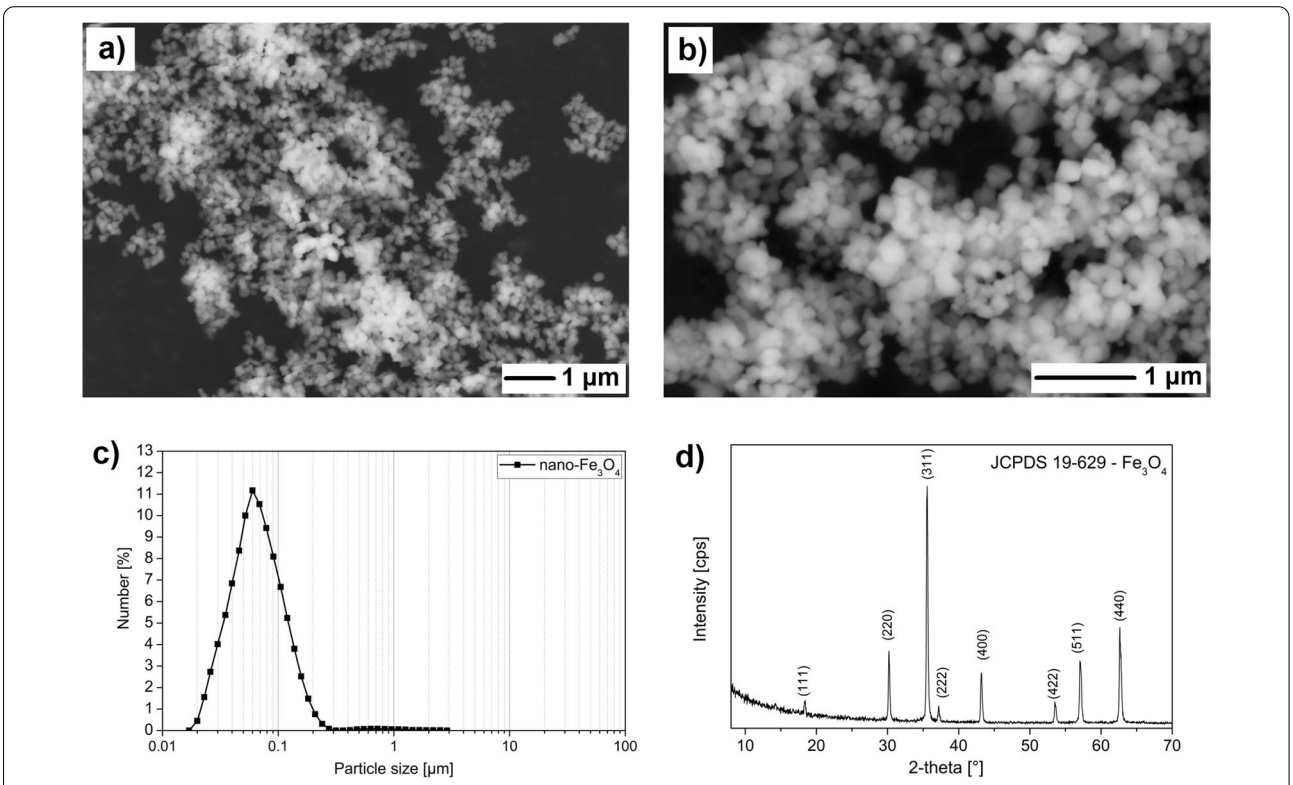


**Fig. 1** SEM micrographs (**a**–**b**), particle size distribution obtained by laser diffraction (**c**) and nanomagnetite powder XRD pattern (**d**)

### 2.2 Mixture Design

Six different cement paste mixtures, with a fixed water-to-binder (w/b) ratio of 0.4, were produced. This included a plain control paste designated as NM0. 5 series of cement pastes, containing 5, 10, 15, 20 and 30 wt% of nano-$Fe_3O_4$ as a cement replacement and designated as NM5, NM10, NM15, NM20 and NM30, respectively, were produced. Their mixture compositions are summarized in Table 3.

### 2.3 Specimen Preparation

The cement paste specimens used in this study were prepared using a standard mixer, complying with EN 196–1. All of them were mixed using the following procedure: (1) slow mixing—30 s, (2) fast mixing—1 min, (3) pause—1 min, (4) fast mixing—1 min. The nano-modified specimens ($Fe_3O_4$ NPs) were dry mixed for 30 s to ensure a homogeneous distribution of dry materials. After mixing, $20 \times 20 \times 20$ $mm^3$ cubic specimens were cast for compressive strength and radiation shielding evaluations. After casting, they were kept in a climate chamber, at room temperature ($20 \pm 1$ °C) and at a relative humidity of 95%, until the day of testing.

## 3 Methods

Rheological measurement was performed using an MCR 301 (Anton Paar) stress-imposed rheometer, equipped with calibrated helicoidal geometry (Liard et al. 2015; Olivas et al. 2017) specially designed for cementitious materials (Ojeda-Farías et al. 2019). The following procedure was applied: (i) pre-shearing for 10 s at a constant shear-rate of 100 $s^{-1}$; (ii) determination of shear stress as a function of shear rate, from 100 $s^{-1}$ to 0.1 $s^{-1}$, with 30 points distributed evenly along a logarithmic scale, for a total of 300 s.

The early strength evolution of the cement pastes was determined based on an ultrasonic wave reflection method, using a compact 8-cell ultrasonic device (Sonomed, Poland) containing three ultrasonic shear wave transducers bonded to one waveguide per cell (Lootens et al. 2020; Meacci et al. 2016). This device was used to measure the reflection loss coefficient of a reflected wave, generated at the interface of a waveguide and a hydrating cement paste. Afterward, the shear modulus of the specimen was estimated from this measurement, which is related to the elastic modulus and, ultimately, compressive strength. The early strength at selected time intervals can thus be calculated. Strengths after 24, 48, and 72 h are presented below.

Compressive strength was determined on six specimens of each series, after 7 and 28 days of curing, using a Toni Technik (Zwick Roell, Germany) testing machine. The mean value of each of the 6 samples was taken as representative.

A MIP test was performed after 28 days of curing, with the use of Pascal 140 and 240 series (Thermo Scientific) mercury intrusion porosimeters. Prior to testing, small-cored specimens taken from the samples were immersed in isopropanol and then freeze-dried to stop hydration. The mercury density was 13.55 g/mL, the surface tension was taken as 0.48 N/m, while the selected contact angle was 140°.

The macroscopic cross-section of slow neutrons ($\Sigma_S$), linear attenuation coefficients (LACs), and kerma coefficients of the γ-ray, were determined experimentally. For slow neutron transmission measurements, an $^{241}$Am–Be neutron source with an activity of 3.7 GBq and a neutron yield = (1.1–1.4) $10^7$ n/s was utilized for sample irradiation. The gamma-ray transmission measurements were performed with three γ-ray point sources – $^{131}$Ba, $^{137}$Cs and $^{60}$Co –, which emit six γ-ray lines at 80, 238.63, 662, 911, 1173.23 and 1332.49 keV. These energies were used for sample irradiation and calibration of the detection system. A $2'' \times 2''$ NaI (TI) inorganic crystal, coupled with a multi-channel analyzer (MCA), was used to record the incident and transmitted γ-ray spectra. The resolution of the gamma-ray spectrometer was 12.5% at 662 keV. The neutron and gamma-ray measurements were repeated three times for each thickness, with the average value reported. The estimated errors for all the radiation measurements were less than 5%.

Furthermore, theoretical values for the macroscopic cross-sections of fast and thermal neutrons were calculated using the NXcom program (El-Khayatt 2011) and of the online calculator build by (Kienzle 2019), respectively. The details of measuring technique including description of experimental set-up can be found in previous work of authors Sikora et al., (2021b).

**Table 3** Cement paste mix design

| Sample designation | Cement [g] | Water [g] | $Fe_3O_4$ nanoparticles [g] |
|---|---|---|---|
| NM0 | 1000 | 400 | - |
| NM5 | 950 | 400 | 50 |
| NM10 | 900 | 400 | 100 |
| NM15 | 850 | 400 | 150 |
| NM20 | 800 | 400 | 200 |
| NM30 | 700 | 400 | 300 |

## 4 Results and Discussion

### 4.1 Rheology

The rheological measurements were performed directly after mixing. The curves obtained were fitted to a Herschel–Bulkley equation $\tau$, which fit the experimental

data perfectly (Herschel & Bulkley 1926). The evolution of the shear stress of the different mixes, as a function of shear rate, can be observed in the left graph of Fig. 2. All curves displayed a non-zero shear stress value when the shear rate approached zero. This value, also called the yield stress, is depicted in the right graph of Fig. 2 as a function of the $Fe_3O_4$ content. The presence of yield stress is expected in cement paste without plasticizer because of the attractive interactions between cement particles (Nägele 1985).

As can be seen, the higher the $Fe_3O_4$ content, the higher the measured viscosity and yield stress. This is an interesting result, as the impact of a particle's substitution can be difficult to predict. Indeed, for a hard sphere, combining particles of different sizes increases the maximum packing fraction of the total population (Farr & Groot 2009), which leads to better flow properties. Moreover, in this case, the substitution was done per mass of particles and therefore, the volume of nano-$Fe_3O_4$ added was lower than the substituted volume of cement paste, leading to a decrease in the volume fraction with the nano-$Fe_3O_4$ content. These two findings would predict a decrease in viscosity with the substitution of cement. Nevertheless, nano-$Fe_3O_4$ particles are much smaller than cement particles, leading to the measured surface area being significantly higher than in the case of cement. This substantial increase in the surface area should induce an increase in yield stress (Ferraris et al. 2001). The experimental results showed that viscosity increased with the degree of substitution, proving that surface effects (absorption, interaction, etc.) were predominant.

### 4.2 Cement Paste Density

Fig. 3 depicts the influence of nano-$Fe_3O_4$ on cement paste density. It is clear that the density increment was positively proportioned to the nano-$Fe_3O_4$ powder content. This was expected, as $Fe_3O_4$ NPs have a substantially higher specific gravity than cement. As such, nanomagnetite-modified pastes exhibited up to 14.8% higher densities (NM30). Moreover, the ultra-fine size of the nanomagnetite particles lead them to fill the voids between the cement particles, thus improving packing and sample density.

### 4.3 Mercury Intrusion Porosity (MIP)

The experimental results of MIP measurements, at the age of 28 days, are presented in Table 4. The replacement of cement with nano-$Fe_3O_4$ resulted in a gradual

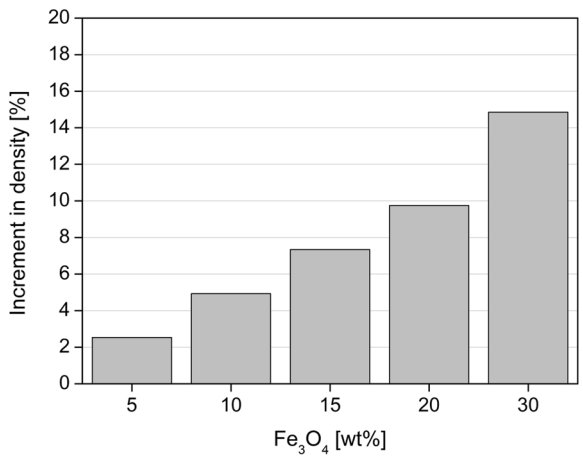


**Fig. 3** Percentage density increment in specimens containing nano-$Fe_3O_4$, in comparison with pristine (NM0) cement paste

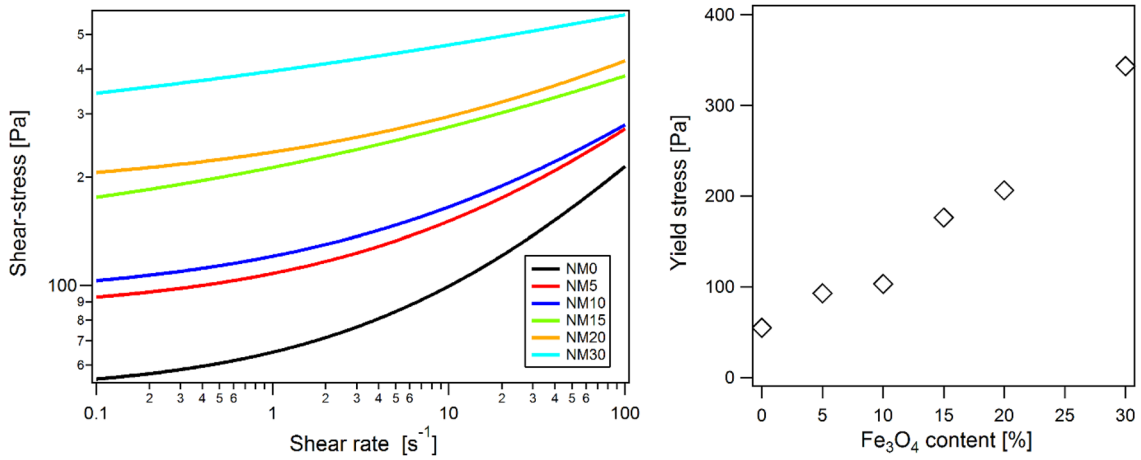


**Fig. 2** Shear-stress as a function of the shear rate of cement pastes (left) and yield stress at 0.1 $s^{-1}$ as a function of the nanomagnetite dosage (right)

**Table 4** Basic parameters of pore structure measured by MIP

| Sample designation | R | NM5 | NM10 | NM15 | NM20 | NM30 |
|---|---|---|---|---|---|---|
| Porosity by Hg intrusion [vol%] | 21.09 | 23.3 | 26.29 | 27.09 | 26.46 | 29.12 |
| Total pore volume [$mm^3/g$] | 121.00 | 135.31 | 146.21 | 158.47 | 153.07 | 166.85 |
| Average pore diameter [nm] | 40.12 | 41.52 | 46.01 | 44.42 | 41.29 | 45.28 |
| Median pore diameter [nm] | 85.65 | 85.99 | 92.38 | 95.28 | 83.64 | 91.81 |

increment in the total porosity of the cement matrix, as well as an increase in average and median pore sizes. The porosities of NM5, NM10, NM15, NM20, and NM30 were 11%, 25%, 28%, 25%, and 38% higher than the value reported for the NM0 paste, respectively. It is widely agreed that porosity is a critical cement matrix characteristic affecting the strength and durability of cement-based materials (Strzałkowski & Garbalińska 2020). Therefore, the observed alteration in porosities resulting from the cement replacement with $Fe_3O_4$ NPs, is in good correlation with the compressive strength values ("Compressive strength"). Despite the importance of the total porosity of a cement matrix concerning the mechanical and physical properties of cement-based composites, the principal governing factor here is the volume of pores in a certain diameter range. Fig. 4 presents the pore size distribution of the cement pastes used in this experiment. The present study confirms that specimens with higher $Fe_3O_4$ NP contents (NM10, NM15, NM20, NM30) are characterized by a higher contribution of harmful pores (>0.2 μm). Therefore, the MIP study proves that both (1) agglomeration of $Fe_3O_4$ NPs in the cement matrix and (2) a higher free water content, resulting from a lower amount of cement in the $Fe_3O_4$-modified pastes, have negative effects on the porosity characteristics of cement pastes, thus resulting in a substantial compressive strength reduction in modified pastes.

### 4.4 Early Strength Development (Ultrasonic Evaluations)

Fig. 5 depicts pastes' early strength values, determined after 24, 48, and 72 h. The early strength development of cement pastes containing nano-$Fe_3O_4$ decreased with an increase in nanoparticle dosage. A gradual decrement in strength, with an increment of nano-$Fe_3O_4$ cement replacement, is visible. After the first 24 h of cement hydration, the NM30 specimen exhibited 33% lower compressive strength than pristine NM0 paste. The difference between the compressive strength of pristine specimens and those containing $Fe_3O_4$ NPs, increased with hydration time. The impeded strength development of $Fe_3O_4$-modified specimens, was a result of the decreased amount of cementitious material. Accordingly, after 72 h, NM5, NM10, NM15, NM20, and NM30 exhibited 16%, 30%, 31%, 39%, and 47% lower compressive strengths, respectively, than the pristine NM0 specimen.

### 4.5 Compressive Strength

Fig. 6 presents the results of compressive strength tests, undertaken after 7 and 28 days. Similarly to early

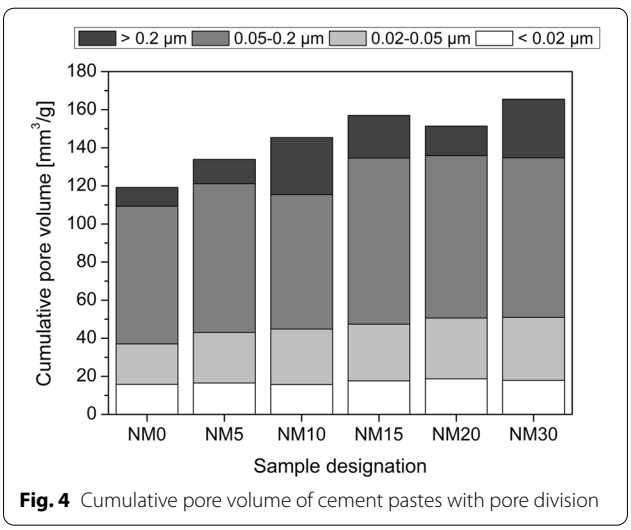


**Fig. 4** Cumulative pore volume of cement pastes with pore division

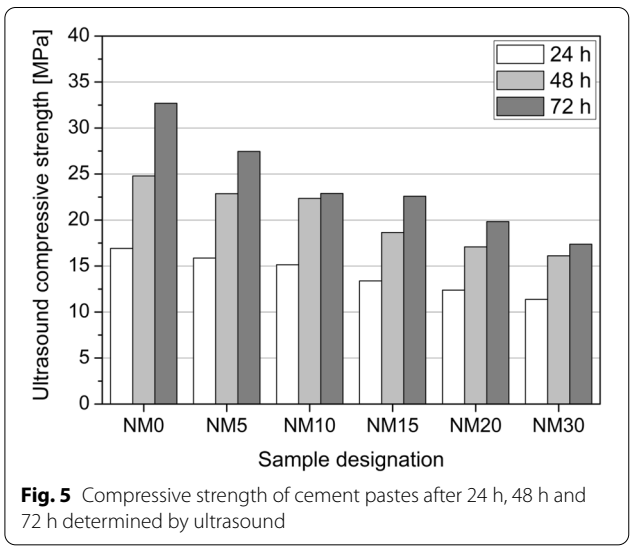


**Fig. 5** Compressive strength of cement pastes after 24 h, 48 h and 72 h determined by ultrasound

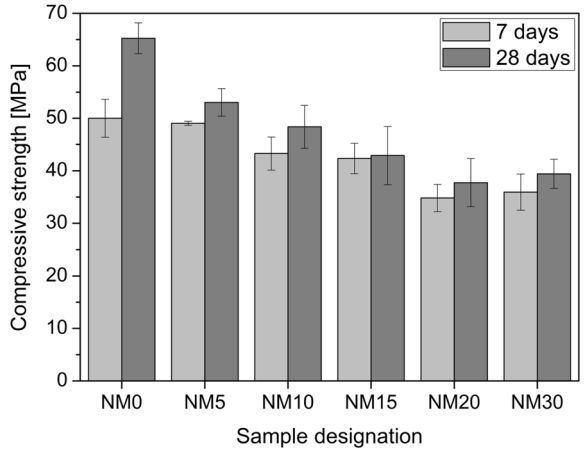


**Fig. 6** Compressive strength of cement pastes after 7 and 28 days of curing

compressive strength test results ("Mercury intrusion porosity (MIP)"), a gradual compressive strength decrement was visible with an increase in nano-$Fe_3O_4$ content. After 7 days of curing, the NM5 specimen exhibited a value comparable to that of NM0, while the incorporation of higher nano-$Fe_3O_4$ contents resulted in gradual strength decrements. The NM30 specimen exhibited 28% lower compressive strength than NM0, after 7 days of curing. After 28 days of curing, the discrepancy between pristine NM0 and all nanomagnetite-modified specimens was more noticeable. NM5, NM10, NM15, NM20, and NM30 exhibited 19%, 26%, 34%, 42%, and 40% lower compressive strengths than the pristine NM0 specimen, respectively. The replacement of cement with high dosages of $Fe_3O_4$ NPs therefore had a negative effect on early strength development, as well as on the 28-day strength of cement pastes.

To date, limited knowledge on the effects of high dosages of $Fe_3O_4$ NPs is available in the literature. Based on previous research (Ghazanlou et al. 2020; Horszczaruk 2019; Mansouri et al. 2019; Seifan et al. 2020), substantial improvements in the mechanical strength of cementitious composites can be obtained when the dosage of nanomagnetite does not exceed 5 wt% of the binder. This effect is mainly attributable to the seeding effect of dispersed $Fe_3O_4$ NPs, as well as to the so-called nano-filling effect of dispersed NPs, which refines the cement matrix and improves its compactness. However, the incorporation of higher dosages of nano-$Fe_3O_4$ results in the creation of particle agglomeration due to strong Van der Waals forces, which increases with a reduction in particle size. This, in turn, results in the formation of specimen heterogeneity and an increment in matrix porosity ("Mercury intrusion porosity (MIP)") and, thus a decrement in mechanical strength. XRD analysis performed by Florez et al. (2019) confirms that high dosages of nano-$Fe_3O_4$ do not affect the main hydration products (i.e., it does not interact chemically with the cement matrix). The replacement of cement with nano-$Fe_3O_4$, therefore, impedes the cement hydration process as a result of the lower cement content in the cement paste.

Florez et al. (2019) have reported an improvement in cement pastes' compressive strength with up to 20 wt% $Fe_3O_4$ NPs. However, they found that the compressive strength of the cement paste was lower than that of pristine specimens at replacement levels of 40 wt% and 50 wt%. Nevertheless, these results are not directly comparable to the present study's results due to differences in mixture design. In the study mentioned above, nano-$Fe_3O_4$ was not considered as a part of the binder material, and the water-to-cement (w/c) ratio was set at a fixed value. Water volume therefore decreased proportionally with cement content, as the nano-$Fe_3O_4$ dosage was increased. In Seifan et al. (2020) study, an improvement in the splitting tensile and compressive strength of cement mortars containing 5 wt%, 10 wt%, and 15 wt% of nano-$Fe_3O_4$ replacement, was reported. However, they found that cement mortars performed best in the

**Table 5** Experimental slow neutron macroscopic cross-sections and calculated effective removal cross-section of fast and thermal neutrons, with their corresponding HVLs

| Sample designation | $\sum_s$ cm$^{-1}$ | HVL (cm) | $\sum_R$ cm$^{-1}$ | HVL (cm) | $\sum_{th}$ cm$^{-1}$ | HVL (cm) |
|---|---|---|---|---|---|---|
| NM0 | 0.2853±0.0143 | 2.43±0.09 | 0.1622 | 4.27 | 0.0649 | 10.68 |
| NM5 | 0.3656±0.0183 | 1.90±0.08 | 0.1726 | 4.02 | 0.0750 | 9.24 |
| NM10 | 0.3982±0.0199 | 1.74±0.07 | 0.1735 | 4.00 | 0.0831 | 8.34 |
| NM15 | 0.4339±0.0217 | 1.60±0.06 | 0.1741 | 3.98 | 0.0910 | 7.61 |
| NM20 | 0.4594±0.0230 | 1.51±0.06 | 0.1745 | 3.97 | 0.1000 | 6.93 |
| NM30 | 0.5219±0.0261 | 1.33±0.05 | 0.1749 | 3.96 | 0.1131 | 6.13 |
| Diff.%[a] | 83.1 | − 82.7 | 7.8 | − 7.8 | 74.3 | − 74.2 |

[a] $Diff.[\%] = 100 \times (NM30 - NM0)/NM30$

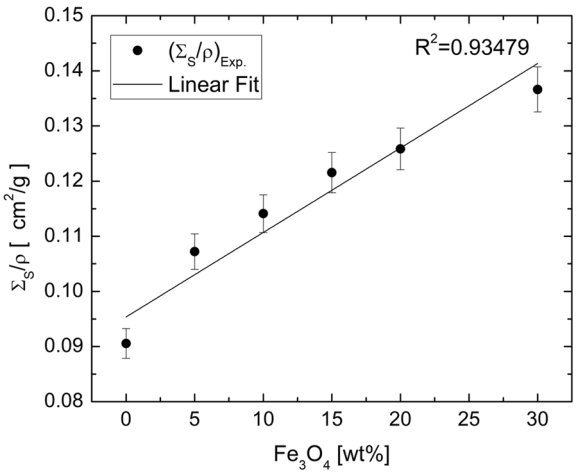


**Fig. 7** Variations of slow neutron cross-section with increasing $Fe_3O_4$ nanoparticles

case of 5 wt%, followed by 10 wt%. In the case of 15 wt%, only minimal compressive strength improvements were reported, with the splitting tensile strength found to be lower than that of the pristine specimen.

### 4.6 Slow, Fast and Thermal Neutron Attenuation Measurements

Table 5 shows the experimental macroscopic cross-sections of slow neutrons (in cm$^{-1}$), as a function of nanomagnetite content. The sample containing $Fe_3O_4$ nanoparticles exhibited a significant increase in slow neutron macroscopic cross-sections, with a difference up to 83.1%, compared to plain cement paste NM0. Additionally, the half-value layer ($HVL = ln2/\sum_S$) results confirmed the positive influence of the $Fe_3O_4$ NPs on the reduction of HVL.

The slow neutron attenuation properties are also shown in Fig. 7, which display a linear relationship between the $Fe_3O_4$ wt% and the mass attenuation cross-section of the slow neutron, $\sum_S/\rho$ (in cm$^2$/g). Addition of nano-$Fe_3O_4$ lead to an increase in the attenuation of slow neutron.

Theoretical fast neutron removal cross-sections ($\sum_R$) for each specimen were determined with the aid of the program NXCom (El-Khayatt 2011), while the total macroscopic cross-section of the thermal neutron ($\sum_{th}$), at 25 meV, was calculated with the help of "Kienzle" online calculator (Kienzle 2019). The elemental weight fractions of the paste mixtures were used as an input data file for running the NXCom and the Kienzle online calculator.

Calculations showed that the addition of magnetite increases both $\Sigma_R$ and $\Sigma_{th}$ and consequently fast and thermal neutron shielding capability, with respect to the plain cement paste, as shown in Table 5. It can be seen that sample NM30 exhibited improved $\Sigma_R$ and $\Sigma_{th}$ values by 74.3 and 7.8%, respectively, when compared to NM0. Similar findings were obtained for the HVL values.

The mass macroscopic cross-section provides a way to distinguish the contributions from chemical composition and density effects. $\Sigma_R/\rho$ and $\Sigma_{th}/\rho$ are depicted in Fig. 8, in which the density effect does not reflect in the plots since all cross-section values were normalized relative to sample density. Therefore, the prime effect of hydrogen on the macroscopic removal cross-section has been observed as a reduction in the $\Sigma_R/\rho$ of the composites with lower hydrogen contents (Additional file 1: Table S1).

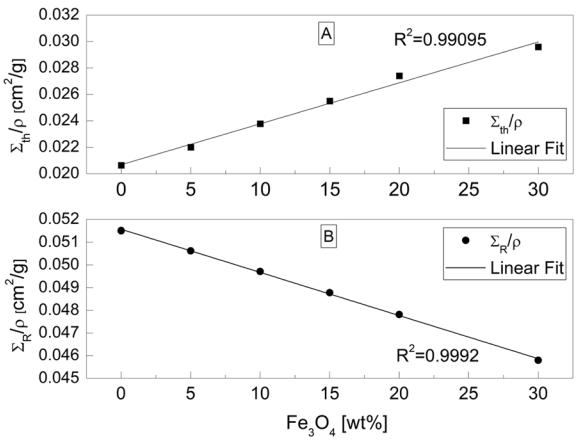


**Fig. 8** Variations of **A** thermal neutron cross-section and **B** fast neutron removal cross-section with increasing $Fe_3O_4$ nanoparticles

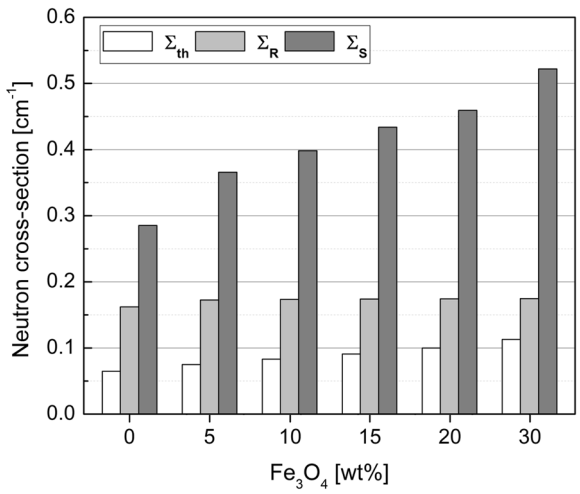


**Fig. 9** Fast, slow, and thermal neutron macroscopic cross-sections for all cementitious matrices

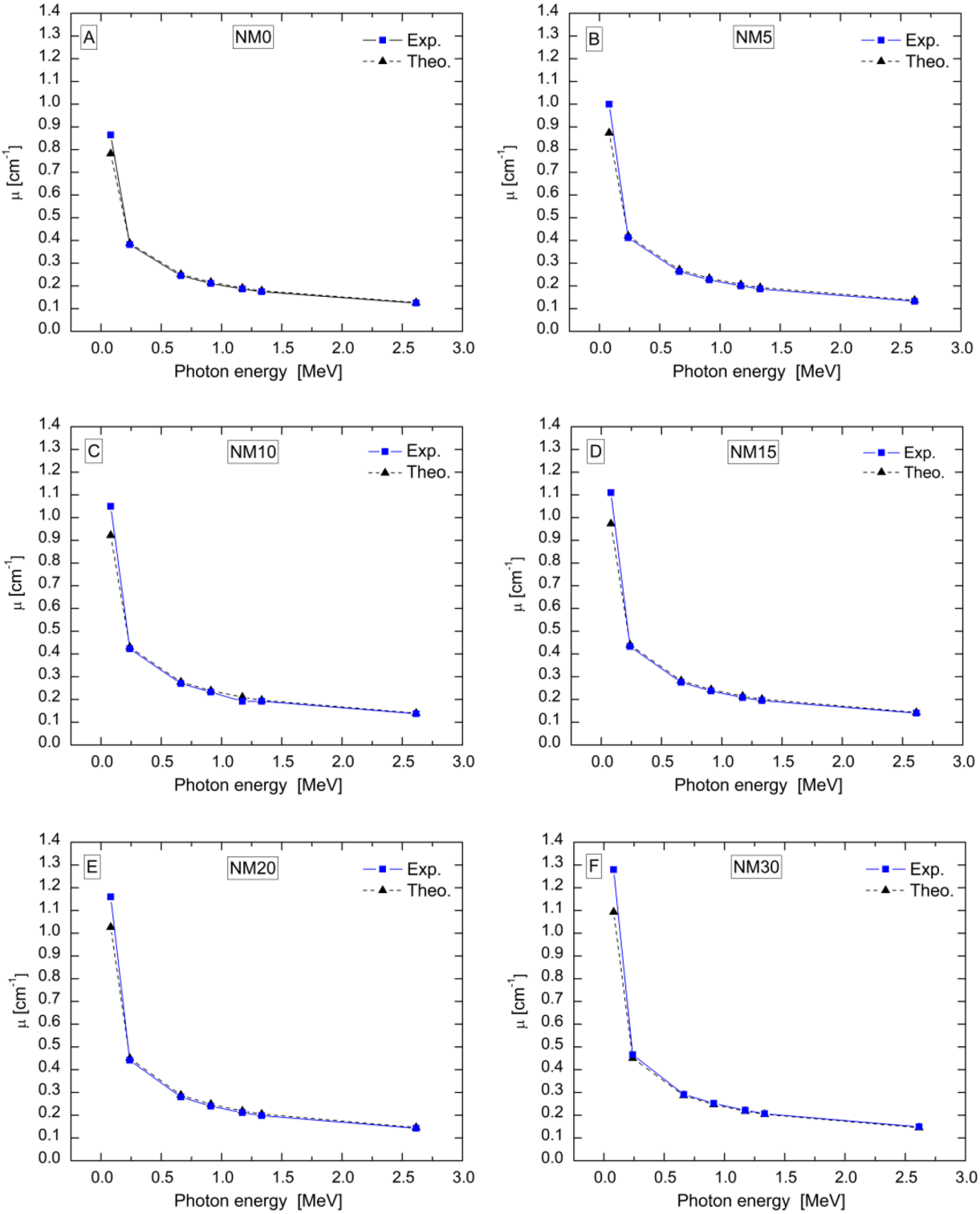


**Fig. 10** Experimental and theoretical linear attenuation coefficients of **a** NM0, **b** NM5, **c** NM10, **e** NM15, **e** NM20 **f**, and NM30 **g** as a function of photon energy

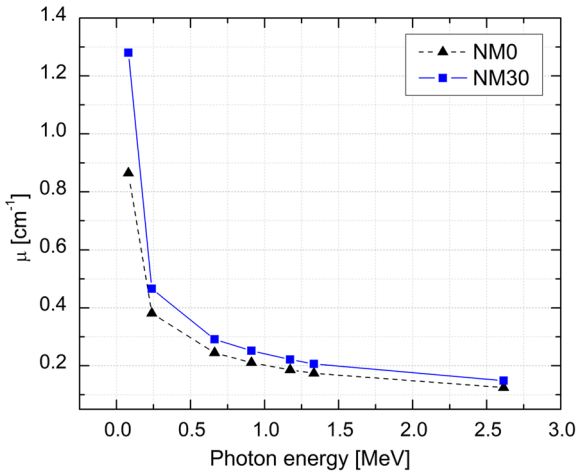


**Fig. 11** Experimental linear attenuation coefficients of NM30 and NM0 as a function of photon energy

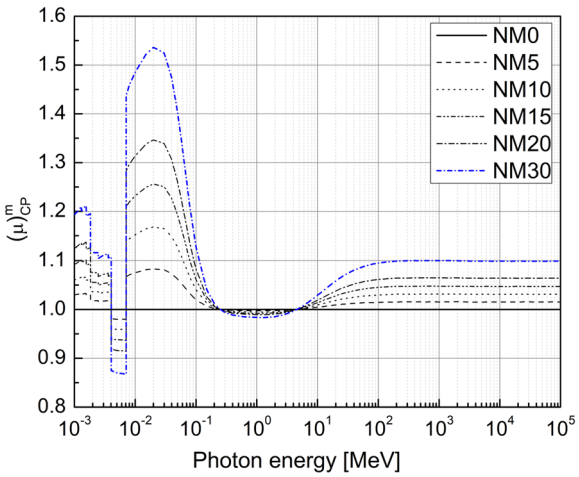


**Fig. 12** The normalized linear attenuation values with respect to the control paste

An overall view of the incorporation of nano-$Fe_3O_4$ into the cementitious matrix for neutron shielding is presented by the bar chart in Fig. 9. It simultaneously depicts the macroscopic cross-sections for the three neutron energy regions: thermal, fast, and slow. As shown in the figure, the inclusion of $Fe_3O_4$ nanoparticles in the cementitious matrix enhances neutron shielding ability, especially for slow neutrons.

### 4.7 Gamma-ray Linear Attenuation Coefficients

The experimental linear attenuation coefficients μ of the cement pastes were determined at photon energies of 80, 238, 662, 911, 1173.2, 1332.5 and 2614 keV. The experimental and theoretical data are depicted in Fig. 10, and presented in Additional file 1: Table S2. All experimental and calculated values agree well, even though the attenuation coefficient at 80 keV was not well-predicted. This was due to the dominance of the photoelectric absorption process, which is prone to error in elemental analysis and heavily affected by the homogeneity of the sample under investigation.

The results obtained show that all the samples′ linear attenuation coefficients displayed the same downward trend with increasing photon energy, exactly as expected. Specifically, the γ-ray attenuation decreased dramatically from 80 to 238 keV, which decreased slowly, as shown in Fig. 10. This observed behavior can be attributed to the dominance of photoelectric and Compton interactions in the low and intermediate energies, respectively.

For comparison purposes, the experimental linear attenuation coefficients of NM30, containing the largest nanoparticle magnetite content, and the control paste (NM30), are depicted in Fig. 11.

For the quantitative comparison task, the linear attenuation coefficient ratio of a given paste material and that of the control paste, NM0, is given in Fig. 12. The comparison results reveal that cement pastes with nanosized magnetite exhibit higher linear attenuation coefficients than the than plain NM0 paste (Fig. 11). For example, in the case of NM30, at low photon energies (20 keV) the difference was over 150%, while in the high photon energies (≥ 100 MeV), it was over 10%, in comparison to NM0. However, Fig. 12 also shows that there was no significant variation at the intermediate photon energies (around 1 MeV), due to the addition of magnetite nanoparticles. This is due to the dominance of the Compton scattering interaction with slightly dependence on the elemental atomic number Z.

Fig. 13 shows the variation of the linear attenuation coefficient of the cement paste as a function of $Fe_3O_4$ nanoparticle content for two dominant regions: (A) the photoelectric region and (B) Compton scattering region. The relationships are linear, not only for the photoelectric region but also for the Compton region, with the gradient of the fitting line decreasing with an increase in photon energy.

### 4.8 Gamma-ray Kerma Coefficients

The experimental kerma coefficient, *k*, of the cement pastes was determined at the listed energies in Table 6. Furthermore, the kerma coefficient–photon energy dependence of the control paste and the paste loaded with the highest amount of nanomagnetite, NM30, is

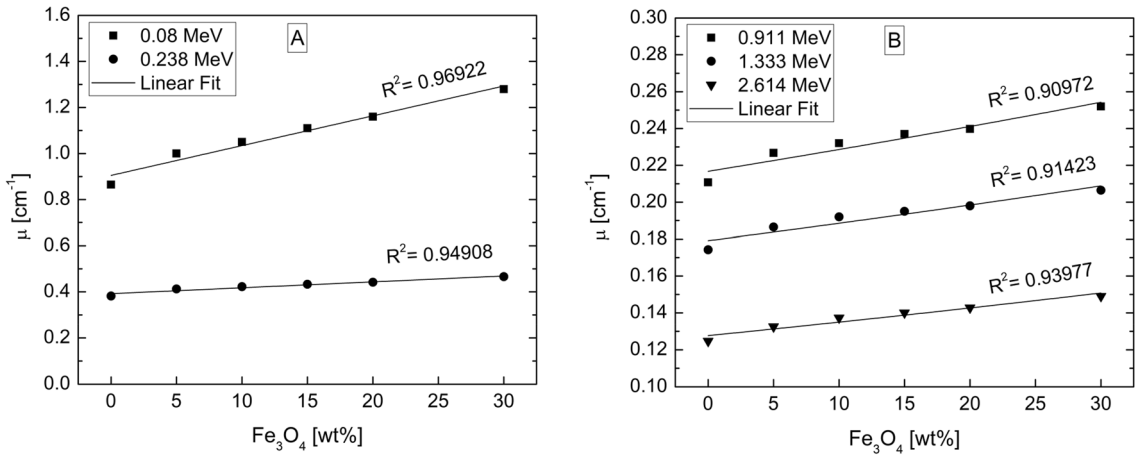


**Fig. 13** The linear attenuation coefficient of $Fe_3O_4$ nanoparticle cement paste, as a function of the weight percentage of $Fe_3O_4$, for two dominant regions: **a** the photoelectric absorption and **b** Compton scattering interaction

plotted in Fig. 14. As can be seen, very good agreement between the theoretical results and the experimental data was achieved.

It can be seen that the energy dependence of *k* is characterized by two distinct energy regions: the first with energies below approximately 150 keV, and the second beyond 150 keV. They seem to form continuation regions, which have a tendency for rapid decrease, and increase in the kerma coefficient, respectively. All *k*-graphs have a dip around 150 keV and higher additions of nanosized magnetite enhanced the K- and the L-absorption edges Table 6.

Normalized kerma coefficients, with respect to the NM0 specimen are presented in Fig. 15. It can be clearly seen that *k* increased with increasing $Fe_3O_4$ content, with the maximum differences among the various pastes noticeable at the 50-keV photon energy level. Finally, the results show that the inclusion of nanosized magnetite powder produced cement paste with highly improved gamma shielding performance.

## 5 Conclusions

This study aimed at developing a lead-free cement paste material for radiation shielding purposes. The following conclusions can be put forward:

1) Paste rheology is significantly affected by the addition of nanomagnetite powder. Thanks to a higher surface area and the finer particle size of $Fe_3O_4$ NPs, in comparison to cement particles, their yield stress and viscosity increase with nanomagnetite powder content in the cement paste.
2) Replacement of cement with nano-$Fe_3O_4$ powder impedes the early strength development of cement pastes, as well as their 7- and 28-day compressive

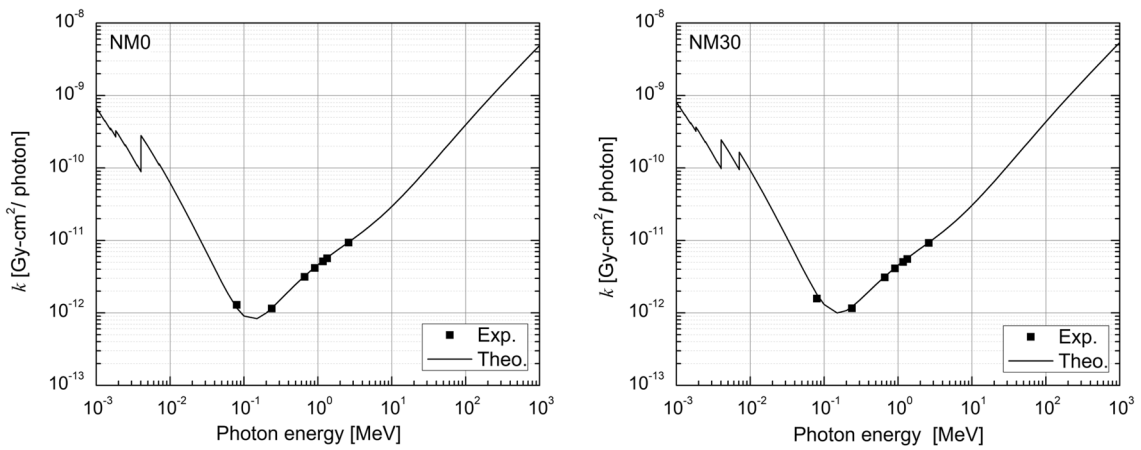


**Fig. 14** Kerma coefficients for NM0 (left) and NM30 (right) cement pastes

**Table 6** Measured and theoretical kerma coefficients (*k*, pGy.cm$^2$/photon) of cement pastes modified with $Fe_3O_4$ nanoparticles. The experimental error was less than 5%

| Energy (keV) | NM0 | | NM5 | | NM10 | | NM15 | | NM20 | | NM30 | |
|---|---|---|---|---|---|---|---|---|---|---|---|---|
| | Exp | Theo | Exp | Theo | Exp | Theo | Exp | Theo | Exp | Theo | Exp | Theo |
| 80 | 1.29 | 1.17 | 1.38 | 1.26 | 1.41 | 1.37 | 1.46 | 1.47 | 1.49 | 1.58 | 1.57 | 1.80 |
| 238 | 1.15 | 1.17 | 1.15 | 1.17 | 1.15 | 1.18 | 1.15 | 1.19 | 1.15 | 1.20 | 1.16 | 1.21 |
| 662 | 3.14 | 3.22 | 3.12 | 3.22 | 3.13 | 3.21 | 3.12 | 3.20 | 3.10 | 3.19 | 3.08 | 3.18 |
| 911 | 4.16 | 4.28 | 4.14 | 4.27 | 4.14 | 4.26 | 4.13 | 4.24 | 4.09 | 4.23 | 4.11 | 4.21 |
| 1173.3 | 5.13 | 5.26 | 5.09 | 5.24 | 4.77 | 5.23 | 5.06 | 5.22 | 5.02 | 5.20 | 5.03 | 5.17 |
| 1332.5 | 5.65 | 5.80 | 5.59 | 5.79 | 5.62 | 5.77 | 5.58 | 5.76 | 5.54 | 5.74 | 5.52 | 5.71 |
| 2614.0 | 9.34 | 9.51 | 9.17 | 9.50 | 9.28 | 9.48 | 9.26 | 9.46 | 9.23 | 9.44 | 9.21 | 9.40 |

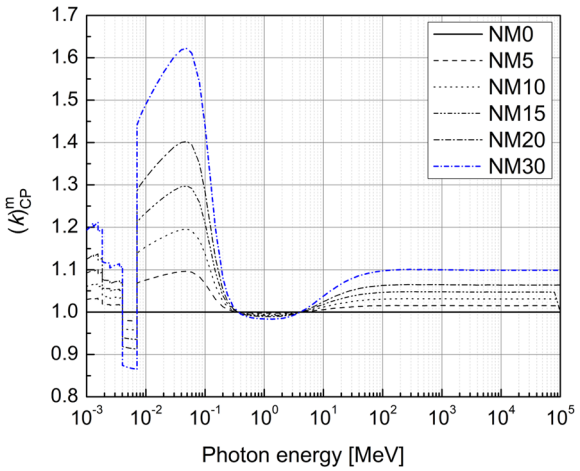


**Fig. 15** The normalized kerma coefficient values, with respect to the control sample

strength. The decrement rate increases gradually with nano-$Fe_3O_4$ content within a specimen.

3) The total porosity and pore size distribution of cement pastes are significantly altered by the addition of high amounts of nanomagnetite particles. Higher contents of $Fe_3O_4$ NPs result in the creation of agglomeration within the cement matrix, which results in an undesirable increment of cement matrix porosity and thus negatively affects the compressive strength of cement pastes.
4) The dry density of cement pastes increases with an increment in the replacement level, owing to the high density of magnetite nanoparticles compared to cement. All macroscopic cross-sections of slow, fast and thermal neutrons are constantly increased by the addition of magnetite nanoparticles, with their variations being markedly linear. The incorporation of 30 wt% of nano-$Fe_3O_4$ (NM30 specimen) therefore, resulted in a decrement in the slow, fast and thermal HVLs by 82.7%, 7.8%, and 74.2%, respectively, when compared to pristine (NM0) paste. Although all neutron cross-sections showed an increasing trend with increasing $Fe_3O_4$, the $\Sigma_s$ results showed distinct rates of increase with magnetite content.
5) Gamma-ray linear attenuation and kerma coefficients exhibit systematic increases with increasing $Fe_3O_4$ content. Except for the values around 1 MeV, no substantial differences were observed between various cement composites. The maximum differences between the kerma and linear attenuation curves were noticed at 50 and 20 keV, respectively. Variations in the linear attenuation coefficient of cement paste, as a function of nanosized magnetite loading for the dominant regions of photoelectric and Compton interactions, are linear.

## Supplementary Information

The online version contains supplementary material available at https://doi.org/10.1186/s40069-022-00568-y.

**Additional file1: Table S1.** Elemental composition and effective removal cross section ($\Sigma_R$%) as a function of magnetite content. **Table S2.** Measured and theoretical linear attenuation coefficients (μ, cm$^{-1}$) of cement pastes modified with $Fe_3O_4$ nanoparticles. The experimental error is less than 5%.

**Acknowledgements**
We would like to thank Dietmar Stephan, Christian Lehmann and David Dahncke from TU Berlin for supporting this research with SEM and MIP measurements.

**Author contributions**
PS: conceptualization, methodology, investigation, validation, visualization, resources, formal analysis, data curation, writing—original draft, writing—review and editing, project administration, funding acquisition, supervision. AEK: methodology, investigation, validation, visualization. formal analysis, data curation, writing—original draft, writing—review and editing, project administration. HAS: methodology, investigation, validation, writing—original draft. ML: methodology, investigation, validation, visualization, writing—original draft. DL: methodology, validation, formal analysis, writing—review and editing, project administration. SYC: investigation, formal analysis, writing—review

and editing, funding acquisition. PW: conceptualization, methodology, investigation, funding acquisition, writing—original draft, writing—review and editing. MAE: methodology, validation, formal analysis, writing—review and editing. All authors read and approved the final manuscript.

**Author information**
P. Sikora: Ph.D., Associate Professor, West Pomeranian University of Technology in Szczecin, Poland. Ahmed El-Khayatt: Ph.D., Professor, Imam Muhammad Ibn Saud Islamic University, Saudi Arabia. H.A. Saudi: Ph.D., Professor, Al-Azhar University, Egypt. M. Liard: Ph.D., Senior Scientist, Sika Technology AG, Switzerland. D. Lootens: Ph.D., Principal Scientist, Sika Technology AG, Switzerland. S.-Y. Chung: Ph.D., Assistant Professor, Sejong University, South Korea. P. Woliński: Ph.D., Assistant Professor, Collegium Mazovia Innovative University, Poland. M. Abd Elrahman: Ph.D., Associate Professor, Mansoura University, Egypt.

**Funding**
This research was funded in part by the National Science Centre, Poland within Project No. 2020/39/D/ST8/00975 (SONATA-16). This work is supported by the Korea Agency for Infrastructure Technology Advancement (KAIA) grant funded by the Ministry of Land, Infrastructure, and Transport (Grant 22NANO-C156177-03).

**Data availability**
The data that support the findings of this study are availablefrom the corresponding author, P.S., upon reasonablerequest.

## Declarations

**Competing interests**
The authors declare that they have no known competing financial interests or personal relationships that could have appeared to influence the work reported in this paper.

**Author details**
[1]Building Materials and Construction Chemistry, Technische Universität Berlin, Gustav-Meyer-Allee 25, 13355 Berlin, Germany. [2]Faculty of Civil and Environmental Engineering, West Pomeranian University of Technology in Szczecin, Al. Piastow 50, 70-311 Szczecin, Poland. [3]Department of Physics, College of Science, Imam Mohammad Ibn Saud Islamic University, (IMSIU), Riyadh, Saudi Arabia. [4]Reactor Physics Department, Nuclear Research Centre, Atomic Energy Authority, Cairo 13759, Egypt. [5]Department of Physics, Faculty of Science, Women Branch, Al-Azhar University, Nasr City, Cairo, Egypt. [6]Sika Technology AG, Sustainability, Zurich, Switzerland. [7]Department of Civil and Environmental Engineering, Sejong University, Seoul 05006, South Korea. [8]Collegium Mazovia Innovative University, Siedlce, Poland. [9]Structural Engineering Department, Mansoura University, Mansoura 35516, Egypt.

Received: 16 July 2022 Accepted: 7 October 2022
Published online: 28 January 2023

**References**

Abo-El-Enein, S. A., El-Hosiny, F. I., El-Gamal, S. M. A., Amin, M. S., & Ramadan, M. (2018). Gamma radiation shielding, fire resistance and physicochemical characteristics of Portland cement pastes modified with synthesized Fe2O3 and ZnO nanoparticles. *Construction and Building Materials, 173*, 687–706. https://doi.org/10.1016/j.conbuildmat.2018.04.071

Akyildiz, A. (2021). Effect of magnetite nanoparticles on cement based composite. *Romanian Journal of Materials, 51*(1), 10–16.

Al-Rajhi, M. A., Idriss, H., Alaamer, A.-A.S., & El-Khayatt, A. M. (2021). Gamma / neutron radiation shielding, structural and physical characteristics of iron slag nanopowder. *Applied Radiation and Isotopes: INcluding Data, Instrumentation and Methods for Use in Agriculture, Industry and Medicine, 170*, 109606. https://doi.org/10.1016/j.apradiso.2021.109606

Amin, M. S., El-Gamal, S. M. A., & Hashem, F. S. (2013). Effect of addition of nano-magnetite on the hydration characteristics of hardened Portland cement and high slag cement pastes. *Journal of Thermal Analysis and Calorimetry, 112*, 1253–1259. https://doi.org/10.1007/s10973-012-2663-1

Amin, M. S., El-Gamal, S. M. A., & Hashem, F. S. (2015). Fire resistance and mechanical properties of carbon nanotubes—clay bricks wastes (Homra) composites cement. *Construction and Building Materials, 98*, 237–249. https://doi.org/10.1016/j.conbuildmat.2015.08.074

Bragança, M. O. G. P., Portella, K. F., Bonato, M. M., Alberti, E., Marino, B., & C. E. (2016). Performance of Portland cement concretes with 1% nano-Fe3O4 addition: electrochemical stability under chloride and sulfate environments. *Construction and Building Materials, 117*, 152–162. https://doi.org/10.1016/j.conbuildmat.2016.05.033

Cendrowski, K., Sikora, P., Zielinska, B., Horszczaruk, E., & Mijowska, E. (2017). Chemical and thermal stability of core-shelled magnetite nanoparticles and solid silica. *Applied Surface Science, 407*, 391–397. https://doi.org/10.1016/j.apsusc.2017.02.118

Dezhampanah, S., Nikbin, I. M., Mehdipour, S., Mohebbi, R., & Moghadam, H. (2021). Fiber- reinforced concrete containing nano - TiO2 as a new gamma-ray radiation shielding materials. *Journal of Building Engineering, 44*, 102542. https://doi.org/10.1016/j.jobe.2021.102542

El-Gamal, S. M. A., Abo-El-Enein, S. A., El-Hosiny, F. I., Amin, M. S., & Ramadan, M. (2018). Thermal resistance, microstructure and mechanical properties of type I Portland cement pastes containing low-cost nanoparticles. *Journal of Thermal Analysis and Calorimetry, 131*, 949–968. https://doi.org/10.1007/s10973-017-6629-1

El-Khayatt, A. M. (2011). NXcom – A program for calculating attenuation coefficients of fast neutrons and gamma-rays. *Annals of Nuclear Energy, 38*, 128–132. https://doi.org/10.1016/j.anucene.2010.08.003

Farr, R. S., & Groot, R. D. (2009). Close packing density of polydisperse hard spheres. *The Journal of Chemical Physics, 131*, 244104. https://doi.org/10.1063/1.3276799

Ferraris, C. F., Obla, K. H., & Hill, R. (2001). The influence of mineral admixtures on the rheology of cement paste and concrete. *Cement and Concrete Research, 31*, 245–255. https://doi.org/10.1016/S0008-8846(00)00454-3

Florez, R., Colorado, H. A., Alajo, A., & Giraldo, C. H. C. (2019). The material characterization and gamma attenuation properties of Portland cement-Fe3O4 composites for potential dry cask applications. *Progress in Nuclear Energy, 111*, 65–73. https://doi.org/10.1016/j.pnucene.2018.10.022

Ghazanlou, S. I., Jalaly, M., Sadeghzadeh, S., & Korayem, A. H. (2020). A comparative study on the mechanical, physical and morphological properties of cement-micro/nanoFe3O4 composite. *Scientific Reports, 10*, 2859. https://doi.org/10.1038/s41598-020-59846-y

He, Y., Lu, L., Sun, K., Wang, F., & Hu, S. (2018). Electromagnetic wave absorbing cement-based composite using Nano-Fe3O4 magnetic fluid as absorber. *Cement and Concrete Composites, 92*, 1–6. https://doi.org/10.1016/j.cemconcomp.2018.05.004

Herschel, W. H., & Bulkley, R. (1926). Konsistenzmessungen Von Gummi-Benzollösungen. *Kolloid-Zeitschrift, 39*, 291–300. https://doi.org/10.1007/BF01432034

Horszczaruk, E., Brzozowski, P., Sikora, P., Cendrowski K., & Mijowska, E. (2017). The Effect of Nanomagnetite on the Shielding Properties of Cementitious Composites. 71st RILEM Annual Week & ICACMS 2017, Chennai, India, 3rd–8th September 2017, 55–61.

Horszczaruk, E. (2019). Properties of cement-based composites modified with magnetite nanoparticles: a review. *Materials*. https://doi.org/10.3390/ma12020326

Jiao, D., Lesage, K., Yardimci, M. Y., El Cheikh, K., Shi, C., & de Schutter, G. (2020). Rheological properties of cement paste with nano-Fe3O4 under magnetic field: flow curve and nanoparticle agglomeration. *Materials*. https://doi.org/10.3390/ma13225164

Jiao, D., Lesage, K., Yardimci, M. Y., El Cheikh, K., Shi, C., & de Schutter, G. (2021). Structural evolution of cement paste with nano-Fe3O4 under magnetic field - Effect of concentration and particle size of nano-Fe3O4. *Cement and Concrete Composites, 120*, 104036. https://doi.org/10.1016/j.cemconcomp.2021.104036

Jóźwiak-Niedźwiedzka, D., Glinicki, M. A., Gibas, K., & Baran, T. (2018). Alkali-silica reactivity of high density aggregates for radiation shielding concrete. *Materials*. https://doi.org/10.3390/ma11112284

Kienzle, P. A. (2019). Extensible periodic table (v1.5.2). *Computer Software*. https://periodictable.readthedocs.io.

Kropyvnytska, T., Sanytsky, M., Rucińska, T., & Rykhlitska, O. (2019). Development of nanomodified rapid hardening clinker-efficient concretes based on composite Portland cements. *Eastern-European Journal of Enterprise Technologies, 6*, 38–48. https://doi.org/10.15587/1729-4061.2019.185111

Lesbayev, A., Elouadi, B., Borbotko, T., Manakov, S., Smagulova, G., Boiprav, O., et al. (2017). Influence of magnetite nanoparticles on mechanical and shielding properties of concrete. *Eurasian Chemico-Technological Journal, 19*, 223. https://doi.org/10.18321/ectj666

Liard, M., Oblak, L., Hachim, M., Vachon, M., & Lootens, D. (2015). Impact of viscosity on hydration kinetics and setting properties of cementitious materials. *Advances in Civil Engineering Materials, 3*, 20130096. https://doi.org/10.1520/ACEM20130096

Lootens, D., Schumacher, M., Liard, M., Jones, S. Z., Bentz, D. P., Ricci, S., et al. (2020). Continuous strength measurements of cement pastes and concretes by the ultrasonic wave reflection method. *Construction and Building Materials, 242*, 117902. https://doi.org/10.1016/j.conbuildmat.2019.117902

Maher, A.E.-T., El-Feky, M. S., Mohsen, A., & Kohail, M. (2021). Properties of nano engineered concrete subjected to accelerated corrosion. *Nanotechnologies in Construction A Scientific Internet-Journal, 13*, 293–305. https://doi.org/10.15828/2075-8545-2021-13-5-293-305

Mansouri, I., Nejat, M., Shahbazi, S., & Karami, A. (2019). Effect of magnetite nanoparticles (ferroferric oxide) on discrete concrete properties. *Proceedings of the Institution of Civil Engineers—Construction Materials, 172*, 95–102. https://doi.org/10.1680/jcoma.17.00055

Meacci, V., Ricci, S., Bruehwiler, A., & Lootens, D. (2016). Compact ultrasound board for measurement of concrete compressive strength. *IEEE International Ultrasonics Symposium (IUS), Tours, France, IEEE, 18.09.2016 - 21.09.2016*, 1–4.

Mohamed, O. A., El-Gamal, S. M. A., & Farghali, A. A. (2022). Utilization of alum sludge waste for production of eco-friendly blended cement. *Journal of Material Cycles and Waste Management, 24*, 949–970. https://doi.org/10.1007/s10163-022-01369-x

Nägele, E. (1985). The zeta-potential of cement. *Cement and Concrete Research, 15*, 453–462. https://doi.org/10.1016/0008-8846(85)90118-8

Ojeda-Farías, O., Hebraud, P., Lootens, D., Liard, M., & Mendoza-Rangel, J. M. (2019). Thixotropy of reactive suspensions: the case of cementitious materials. *Construction and Building Materials, 212*, 121–129. https://doi.org/10.1016/j.conbuildmat.2019.03.319

Olivas, A., Ferraris, C. F., Martys, N. S., George, W. L., Garboczi, E. J., & Toman, B. (2017). *Certification of SRM 2493: standard reference mortar for rheological measurements*. Gaithersburg: National Institute of Standards and Technology.

Othuman Mydin, M. A., Mohd Nawi, M. N., Mohamed, O., & Sari, M. W. (2022). Mechanical properties of lightweight foamed concrete modified with magnetite (Fe3O4) nanoparticles. *Materials*. https://doi.org/10.3390/ma15175911

Piotrowski, T. (2021). Neutron shielding evaluation of concretes and mortars: a review. *Construction and Building Materials, 277*, 122238. https://doi.org/10.1016/j.conbuildmat.2020.122238

Piro, N. S., Mohammed, A. S., & Hamad, S. M. (2021). Multiple analytical models to evaluate the impact of carbon nanotubes on the electrical resistivity and compressive strength of the cement paste. *Sustainability, 13*, 12544. https://doi.org/10.3390/su132212544

Radziejowska, A., Sagan, J., & Sobotka, A. (2021). Technological and organizational problems in the construction of the radiation shielding concrete and suggestions to solve: a case study. *Open Engineering, 11*, 1114–1121. https://doi.org/10.1515/eng-2021-0082

Ramadan, M., El-Gamal, S. M. A., & Selim, F. A. (2020). Mechanical properties, radiation mitigation and fire resistance of OPC-recycled glass powder composites containing nanoparticles. *Construction and Building Materials, 251*, 118703. https://doi.org/10.1016/j.conbuildmat.2020.118703

Saudi, H. A. (2013). Lead phosphate glass containing boron and lithium oxides as a shielding material for neutron-and gamma-radiation. *Applied Mathematics, 1*, 143–146. https://doi.org/10.12691/amp-1-4-7

Seifan, M., Ebrahiminezhad, A., Ghasemi, Y., Samani, A. K., & Berenjian, A. (2018). Amine-modified magnetic iron oxide nanoparticle as a promising carrier for application in bio self-healing concrete. *Applied Microbiology and Biotechnology, 102*, 175–184. https://doi.org/10.1007/s00253-017-8611-z

Seifan, M., Mendoza, S., & Berenjian, A. (2020). Effect of nano and micro iron oxide particles on the workability, strength and absorption rate of cement mortar containing fly ash. *European Journal of Environmental and Civil Engineering*. https://doi.org/10.1080/19648189.2020.1824822

Shaheen, N., Khushnood, R. A., Khaliq, W., Murtaza, H., Iqbal, R., & Khan, M. H. (2019). Synthesis and characterization of bio-immobilized nano/micro inert and reactive additives for feasibility investigation in self-healing concrete. *Construction and Building Materials, 226*, 492–506. https://doi.org/10.1016/j.conbuildmat.2019.07.202

Sikora, P., Cendrowski, K., Horszczaruk, E., & Mijowska, E. (2018). The effects of Fe3O4 and Fe3O4/SiO2 nanoparticles on the mechanical properties of cement mortars exposed to elevated temperatures. *Construction and Building Materials, 182*, 441–450. https://doi.org/10.1016/j.conbuildmat.2018.06.133

Sikora, P., Chougan, M., Cuevas, K., Liebscher, M., Mechtcherine, V., Ghaffar, S. H., et al. (2021a). The effects of nano-and micro-sized additives on 3D printable cementitious and alkali-activated composites: a review. *Applied Nanoscience*. https://doi.org/10.1007/s13204-021-01738-2

Sikora, P., El-Khayatt, A. M., Saudi, H. A., Chung, S.-Y., Stephan, D., & Abd Elrahman, M. (2021b). Evaluation of the effects of bismuth oxide (Bi2O3) micro and nanoparticles on the mechanical, microstructural and γ-ray/neutron shielding properties of Portland cement pastes. *Construction and Building Materials, 284*, 122758. https://doi.org/10.1016/j.conbuildmat.2021.122758

Sikora, P., Horszczaruk, E., Cendrowski, K., & Mijowska, E. (2016). The Influence of nano-Fe3O4 on the microstructure and mechanical properties of cementitious composites. *Nanoscale Research Letters, 11*, 182. https://doi.org/10.1186/s11671-016-1401-1

Ślosarczyk, A., Klapiszewska, I., & Klapiszewski, Ł. (2021). Influence of nanosilica and binary oxide systems on the selected physical and mechanical properties of cement composites. *Physicochemical Problems of Mineral Processing*. https://doi.org/10.37190/ppmp/144184

Strzałkowski, J., & Garbalińska, H. (2020). The effect of aggregate shape on the properties of concretes with silica fume. *Materials*. https://doi.org/10.3390/ma13122780

## Publisher's Note